CRYSTAL GROWTH & DESIGN

pubs.acs.org/crystal

Article

Controlled BZO Nanorod Growth and Improved Flux Pinning in YBCO Films Grown on Vicinal STO Substrates

Moe Moe Aye,* Elmeri Rivasto,* Hannes Rijckaert, Hannu Huhtinen, Isabel Van Driessche, and Petriina Paturi

Cite This: https://doi.org/10.1021/acs.cgd.3c00768

Read Online

ACCESS | Metrics & More | Article Recommendations

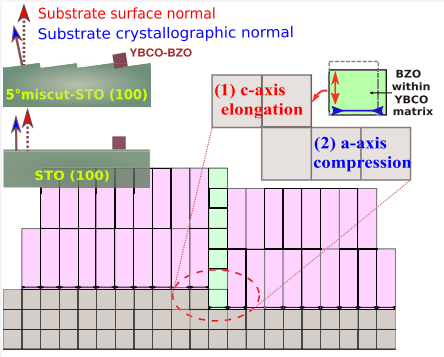

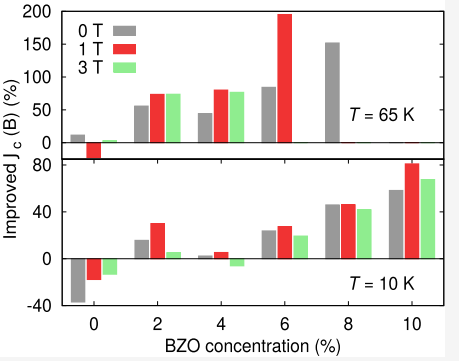

ABSTRACT: The present study systematically investigates the impact of strain-induced defects on the anisotropy of the critical current density across wide temperature and magnetic field ranges. We focus on 0−10 wt % $BaZrO_3$ (BZO)-doped $YBa_2Cu_3O_{7-x}$ (YBCO) thin films that are deposited on $SrTiO_3$ substrates with a 5° surface miscut. Our findings highlight the crucial role played by these vicinal substrates in governing the growth of BZO nanorods within the YBCO films. Interestingly, we observe that the miscut-induced surface step-edge terraces serve as preferred nucleation sites for BZO, resulting in controlled nanorod growth and a significant enhancement in both the self-field and in-field critical current densities. Furthermore, we note that the optimal BZO content for effective flux pinning varies considerably depending on the applied temperature, magnetic field, and its orientation. These findings hold significant implications for the design and development of high-performance superconducting materials. The primary objective in such endeavors is to construct an optimal flux pinning structure that can achieve a high critical current density at relatively high magnetic fields.

INTRODUCTION

In the high-temperature superconductor (HTS) films, the insertion of artificial pinning centers (APCs) within the $YBa_2Cu_3O_{7-x}$ (YBCO) matrix has been shown to have huge potential for a great variety of future power applications.[1−4] Notably, the controllable microstructures that form secondary phase nonsuperconducting flux traps play a crucial role in addressing the issue of excellent flux pinning performance of HTS thin films and coated conductors. For instance, the epitaxially *c*-axis-oriented YBCO films with strongly correlated columnar defects such as $BaZrO_3$ (BZO), $BaSnO_3$ (BSO), or $BaHfO_3$ (BHO) nanorods have been proved to attain the remarkably improved in-field critical current density $J_c(B)$ when the direction of the magnetic field is parallel to the column.[1−6] Moreover, tilted nanocolumns or otherwise mixed APC morphology within the YBCO lattice can reduce the vortex hopping between the defects, increasing J_c in a broad angular range that can lead to improved overall vortex pinning and general angular isotropy, regardless of the direction of the magnetic field.[7−9]

Strain fields play a crucial role in determining the configuration of APC, and it is shown that excessive strain deteriorates superconducting performance, negatively impacting the flux pinning reducing also the self-field critical current density (J_c) in BZO-doped YBCO films.[1,10−14] Since the presence of BZO nanorods together with oxygen nonstoichiometry affects the crystalline quality of YBCO and thus zero field superconducting properties, finding a balance between the maximal crystalline quality and optimal

Received: June 27, 2023
Revised: September 11, 2023

morphology of self-assembled APCs seems to be one of the most important challenges. To achieve the optimal level of strain that can stabilize these conflicting requirements often requires fine-tuning of growth conditions and processing parameters.[15] By utilizing vicinally cut substrates that consist of step-terrace-like surface structure, in place of flat, along STO (100) cut ones, intriguing discoveries have been made regarding the impact of substrate surface morphology on the growth mode and microstructure of YBCO films, offering a promising solution to the problem.[16−24]

The vicinally grown YBCO films exhibit a range of unique phenomena, including lattice misfit-induced defect modifications,[16,25] anisotropic critical current density,[26,27] twin domain modifications,[28] vortex channeling,[29] and *c*-axis tilt alterations due to the combined strain from lattice misfit and surface-step dimensions.[30] Moreover, the interfacial and surface effects at the substrate/film interface can significantly alter the alignment and uniformity of the second-phase nanorod inclusions in the YBCO films, providing a tool to fine-tune the vortex pinning landscape for specific applications.[31,32] It has been found that the superconducting properties are influenced by both lattice misfit strain and surface-step dimensions, where the formation of the nanocolumns further helps to accommodate the strain and to reduce the defect density in the YBCO matrix.[33,34] To gain a comprehensive understanding of the substrate surface's impact on the critical characteristics of YBCO film with regard to the APC concentration, a more systematic investigation of the growth mechanism is necessary.

Motivated by this, we deposited BZO-doped YBCO films of varying BZO concentrations on 5°STO substrates using pulsed laser deposition and investigated the effect of the substrate surface on the crystalline growth of YBCO and formation of BZO nanorods. The superconducting properties were studied in wide temperature and magnetic field ranges, and the results were compared with the detailed structural analysis to understand the growth mechanism and the impact of the lattice strain on the self-field and in-field critical current densities. The comparison sample series was made with the same BZO dopings on the YBCO films grown on typically utilized STO(100) substrates.

EXPERIMENTAL DETAILS

A set of BZO-doped YBCO thin films, with a thickness of ≈190 nm as confirmed by transmission electron microscopy (TEM) measurements, were deposited by pulsed laser deposition (PLD) on STO (100) substrates having a miscut angle of 5° along the [010] direction (Figure 1). BZO-doped YBCO targets with different BZO weight percentages (x = 0, 2, 4, 6, 8, and 10 wt %) were used to introduce APCs in the YBCO matrix. All PLD targets were done by the solid-state reaction method. During the film deposition, all of the critical PLD parameters such as substrate temperature of 750 °C and oxygen partial pressure of 0.17 Torr were taken from our earlier optimizations.[12]

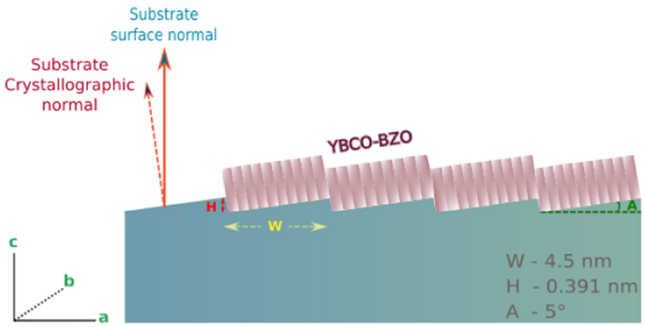

Figure 1. Schematic illustration of a BZO-doped YBCO film grown on a 5°STO substrate.

The structural properties, such as crystal structure, purity, and in-plane and out-of-plane crystallographic orientation of films, were characterized by X-ray diffractometry (XRD). The defect formation and microstructure of films were analyzed by employing Cs-corrected JEOL JEM 2200-FS scanning transmission electron microscopy (STEM) operated at 200 kV with a high-angle angular dark-field (HAADF) detector. Crystallographic information was obtained by high-resolution (HR)-TEM.

The magnetic measurements were performed with a quantum design physical property measurement system (PPMS). The superconducting critical temperature, T_c, and the width of the transition were determined from the ac magnetization in the range 10−100 K (in an ac field of 0.1 mT). From the dc measurement, the magnetic field-dependent critical current density, $J_c(B)$, was calculated according to the Bean model using the opening of the measured hysteresis loop.[35]

Transport properties were measured across the steps of the STO surface via a standard four-probe technique using 50 μm wide bridges made by standard optical lithography. The electrical contacts were made by aluminum wire using a TPT HB05 Wire Bonder and the measurement was done in the PPMS with a horizontal rotator option. The angular-dependent critical current density ($J_c(\theta)$) was measured in a wide range of magnetic fields (B = 0.5, 1, 2, 4, 6, 8 T) and temperatures (T = 10 and 65 K).

RESULTS AND DISCUSSION

Crystalline Quality and Microstructure of the BZO-Doped YBCO Films. High-resolution XRD was employed to investigate the crystalline properties of BZO-doped YBCO films on miscut STO substrates, with a focus on the in-plane and out-of-plane texture evolution of YBCO and BZO dopant in 5°STO films, through various measurements such as (θ−2θ) scan, ω-scan, two-dimensional (2D) (2θ−ϕ) scan, and reciprocal space mapping. As can be seen in Figure 2(a), all of the θ−2θ scans showed only (00l) peaks from YBCO and BZO, proving that the films on 5°STO are fully *c*-axis oriented and epitaxially grown. The offset angle of 5° in the XRD measurements reveals a seamless growth of YBCO with its *c*-axis aligned along the (00l) axis of the STO substrate, affirming that there are no significant crystallographic misorientations between the film and the substrate. In addition, regardless of the substrate, the width of the YBCO (005) peak has an increasing tendency (Table 1), and it is shifted to the lower angles when the BZO content is increased up to 10 wt %, indicating the gradually stretched *c*-axis, as also previously demonstrated in YBCO films on STO substrate.[14] However, in comparison with STO films, the shorter *c*-axis of YBCO in the 5°STO preliminary indicates that the vicinal substrate affects the structural evolution of the deposited film. For example, the lack of clear variation in the position of the BZO (002) peak and the monotonic increase in the width of the 2θ peak with increasing BZO content suggest that the BZO accommodates the coherent strain in the film. Hence, in the vicinally grown films, the strain produced by lattice mismatch between the YBCO and BZO nanorods may slightly tilt the YBCO lattice with respect to the STO substrate normal.[36,37] Therefore, the accommodated unit cells between the film and the terrace of the substrate can lead to combined strain, which can have a significant impact on the structural evolution of BZO nanorods within the YBCO matrix.[16,18,38,39]

https://doi.org/10.1021/acs.cgd.3c00768
Cryst. Growth Des. XXXX, XXX, XXX−XXX

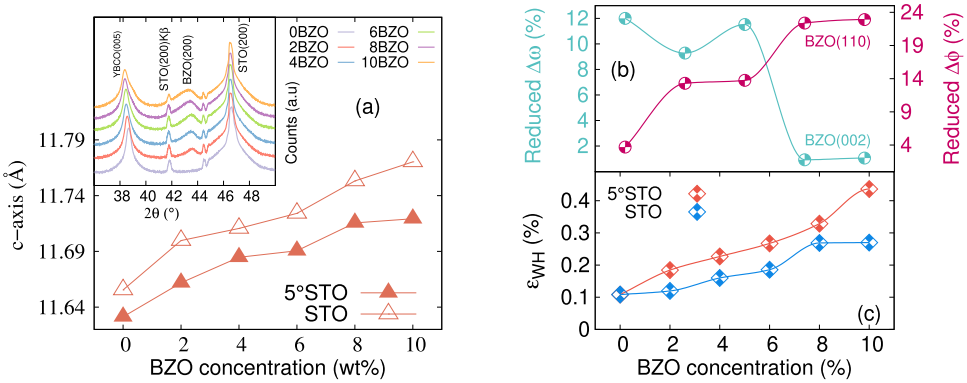

Figure 2. (a) Evolution of *c* lattice parameter with different BZO dopant concentrations for 5°STO and STO films, and the inset figure shows the room-temperature X-ray θ–2θ diffractograms of BZO-doped YBCO films on 5°STO substrates. (b) Reduced variation, $\Delta\omega$(5°STO) − $\Delta\omega$(STO)/$\Delta\omega$(STO), along both out-of-plane and in-plane directions in 5°STO films measured as widths of $\Delta\omega_{005}$ and $\Delta\phi_{102}$ peaks compared with the films grown on STO and (c) the nonuniform microstrain, respectively, when the BZO dopant concentration is increased up to 10%.

Table 1. Structural Properties Determined from the XRD Measurements for BZO-Doped YBCO Samples Deposited on 5° STO and STO Substrates[a]

film	YBCO					BZO	
5°STO	$\Delta\theta_{005}$(deg)	$\Delta\omega_{005}$(deg)	$\Delta\phi_{102}$(deg)	$I(005)/I(004)$	strain(%)	$\Delta\omega_{002}$(deg)	$\Delta\phi_{110}$(deg)
0BZO	0.14	0.49	1.80	15.63	0.11		
2BZO	0.18	0.51	1.83	15.21	0.18	2.01	3.76
4BZO	0.17	0.54	1.84	16.46	0.23	2.13	3.91
6BZO	0.16	0.57	1.85	14.77	0.27	2.30	3.92
8BZO	0.17	0.59	1.87	15.30	0.33	2.44	3.98
10BZO	0.20	0.62	1.91	15.28	0.44	2.44	4.01
STO	$\Delta\theta_{005}$(deg)	$\Delta\omega_{005}$(deg)	$\Delta\phi_{102}$(deg)	$I(005)/I(004)$	strain(%)	$\Delta\omega_{002}$(deg)	$\Delta\phi_{110}$(deg)
0BZO	0.08	0.23	1.88	15.18	0.11		
2BZO	0.11	0.28	1.90	16.41	0.12	2.27	3.90
4BZO	0.11	0.26	1.92	14.74	0.16	2.35	4.51
6BZO	0.10	0.29	1.95	14.64	0.19	2.60	4.55
8BZO	0.21	0.30	1.93	15.53	0.27	2.47	5.12
10BZO	0.21	0.28	1.96	14.97	0.27	2.47	5.21

[a]FWHM of YBCO 2θ(005) peaks ($\Delta\theta_{005}$), FWHM of YBCO(005) rocking curve ($\Delta\omega_{005}$), FWHM of YBCO ϕ(102) peaks, $I(005)/I(004)$, strain values as well as FWHM of BZO (002) rocking curve ($\Delta\omega_{002}$), and FWHM of BZO ϕ(110) peaks.

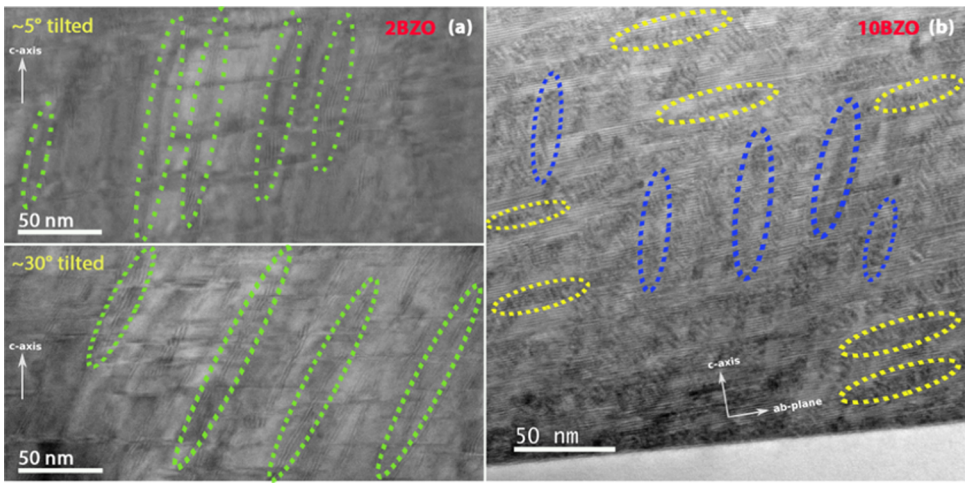

Figure 3. Cross-sectional STEM images of 2 wt % (a) and 10 wt % (b) for the BZO-doped YBCO films deposited on 5°STO substrates. (a) Two examples of differently tilted BZO nanorods in 2BZO film with nanorod tilting angles of 5° (on the top) and 30° (at the bottom), and the white arrow indicates the *c*-axis direction of YBCO. (b) 10BZO films on 5°STO showing a great number of through the film distributed BZO nanorod-like defects lengthened along the in-plane and out-of-plane directions. The examples of these defects are marked with yellow (in-plane) and blue (out-of-plane) ovals. The white arrows indicate the *c*-axis and *ab*-plane directions of YBCO.

https://doi.org/10.1021/acs.cgd.3c00768
Cryst. Growth Des. XXXX, XXX, XXX−XXX

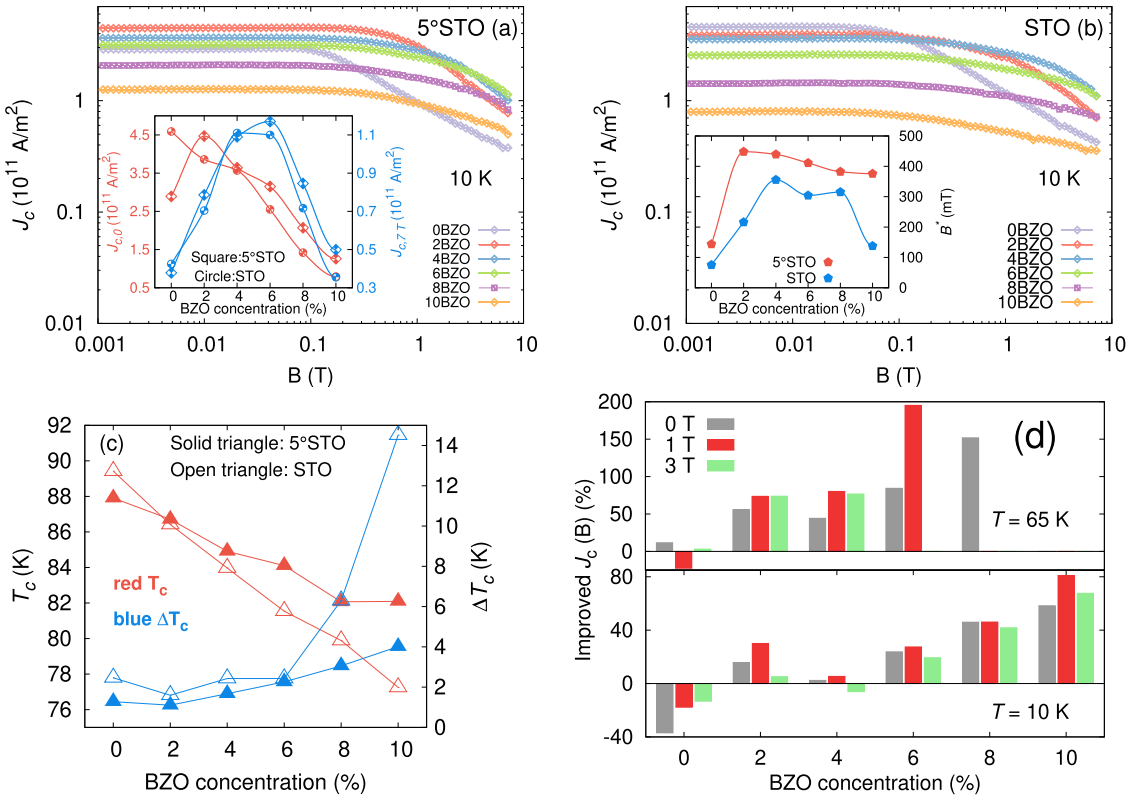

Figure 4. Double-logarithmic plot of the critical current density (J_c) as a function of the applied magnetic field measured at 10 K for 5°STO (a) and STO (b) films. The inset in (a) shows the comparison between the dopant concentration dependence of $J_c(0)$ and the inset in (b) shows the comparison between the dopant concentration dependence of the accommodation field, B^* for BZO-doped YBCO films on 5°STO and STO substrate. (c) Dopant concentration dependence of the critical temperature T_c and the transition width ΔT_c and (d) improvement of J_c in 5°STO samples at temperatures 10 and 65 K in different magnetic fields of 0, 1, and 3 T compared with the values of BZO-doped YBCO films on nonvicinal STO substrate.

When looking at Table 1, the texture of YBCO characterized by the 2D ($2\theta-\phi$) scans of the YBCO (102) peak shows that the difference in the in-plane direction is insignificant and thus the vicinal substrate has no importance in the formation of the low-angle grain boundaries. In addition, based on the intensity ratios between $I(005)/I(004)$ peaks, all of the films regardless of the substrate are similarly oxygenated.[40] Instead, when compared with the films on STO, the broadening of the $\omega(005)$ peak in 5°STO films is striking, the $\Delta\omega$ values are roughly doubled, indicating that the growth of YBCO on the top of the terraces is disturbed leading to clearly weakened out-of-plane ordering of the YBCO unit cells. However, the XRD peaks of BZO in both the in-plane and out-of-plane directions are obviously narrower in the 5°STO films, indicating that the growth of nanorods is clearly improved within the YBCO lattice (Figure 2(b)). As can be seen in Figure 2(c) and in Table 1, an increasing tendency of nonuniform strain in the YBCO lattice with increasing BZO concentration can be in films on both substrates 5°STO and STO. However, at all BZO concentrations, the uniform strain related to XRD peak shift and thus average lattice parameter(Figure 2(a)) is smaller in films on 5°STO, indicating that the use of miscut substrates as a strain mediator may help to alleviate the impact of lattice mismatch-induced strain in BZO-doped YBCO film. Therefore, 5°STO substrate offers a tool to first improve the crystalline quality of BZO-doped YBCO and second further assist the formation of BZO nanorods, having simultaneously a great impact on the self-field $J_c(0)$ and in-field $J_c(B)$.

To understand the effect of the vicinal substrate on the growth of YBCO as well as on the formation of BZO nanorods, HAADF-STEM measurements were applied to the samples 2BZO and 10BZO on 5°STO substrates, as can be seen in Figure 3. In general, the thicknesses of both films are ≈190 nm, and there is a 10 nm thick strained zone next to the substrate interface. When looking at the details of sample 2BZO in Figure 3(a), the YBCO structure is 5° tilted when compared with the STO substrate. This means that also the stacking faults within the YBCO matrix, which are more numerous close to the substrate, are 5° tilted and parallel to the STO substrate surface.

When compared with the BZO-doped films on the STO substrate investigated earlier,[14,41,42] an average diameter of the BZO nanorods here on 5°STO substrate is slightly increased from ≈6 to ≈6.9 nm. In addition, the nanorods are on average longer than in the case of STO substrates, penetrating mainly through the whole film thickness, and they are slightly more randomly distributed, not as homogeneously as in films on STO substrate, though having an average spacing between the nanorods ≈23 nm. The most striking difference compared to the STO substrate is that depending on the location of the film, the nanorods of the 2BZO sample on 5°STO are significantly splayed from the out-of-plane direction of YBCO. The nanocolumns are mostly tilted by 5°, but some nanorods with approximately ≈30° tilt were observed on the top of the strained zones as shown in the bottom left figure.

In the sample with a high BZO concentration of 10 wt % (10BZO) grown on 5°STO, the structure of YBCO is tilted

https://doi.org/10.1021/acs.cgd.3c00768
Cryst. Growth Des. XXXX, XXX, XXX−XXX

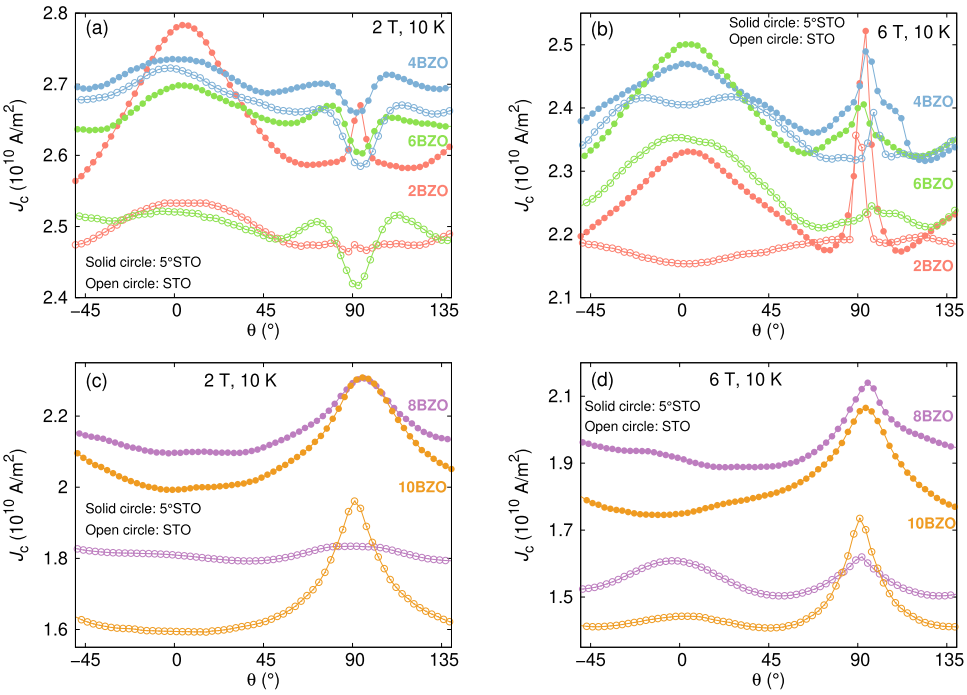

Figure 5. Resistively measured critical current anisotropies for samples with varying BZO concentration at 10 K under applied fields of 2 T (a, c) and 6 T (b, d).

similarly as in the 2BZO sample, 5° compared to the STO substrate. Instead, as can be seen in Figure 3(b), the BZO nanorods are not aligned along the YBCO *c*-axis, but the relatively short BZO nanorods are situated in both in-plane and out-of-plane directions, which could be attributed to the reduced strain field by splaying and/or altering their orientation. As a result, the vicinal films cause a great number of defects throughout the whole film, which, on the other hand, may be the reason for the isotropic enhancement of the superconducting properties.

Strain-Affected Superconducting Properties. Figure 4(c) presents the dopant concentration-dependent onset T_c and transition width ΔT_c for the BZO-doped YBCO films on 5°STO and STO substrates. The T_c of both film sets was observed to decrease in a fairly linear relationship with increasing BZO concentration. This can be linked to the increase in intrinsic strain field with increasing volume fraction of BZO within the YBCO matrix.[15,43] However, the suppression of T_c is clearly smaller in 5°STO, especially at high BZO concentrations, being roughly 5 K higher at 10 wt % BZO than in films on STO. This means that at a high BZO content, the surface terraces may release the strain in the YBCO lattice, thus slowing down the reduction of the T_c. In the 0BZO sample, T_c of 5°STO is slightly reduced when compared with STO, which can be explained by the similar strain-relaxing mechanism that the formation of BZO nanorods can produce. Furthermore, another promising finding in 5°STO films is that the transition width ΔT_c especially in high BZO contents is clearly smaller than that in STO samples. These results suggest that the 5°STO films have slightly better overall crystalline quality when they are doped with BZO.

The main panels of Figure 4(a,b) present double-logarithmic plots for the dependence of J_c on applied magnetic field between 0 and 8 T measured at 10 K for 5°STO and STO samples. As can be seen for 5°STO, a clear overall increase in J_c is observed in 2BZO, 4BZO, and 6BZO samples when compared with sample 0BZO, whereas 8BZO and 10BZO show increased J_c only at high magnetic fields. In 0BZO, $J_c(B)$ is the smallest above 1 T although the J_c is larger than that in 8BZO and 10BZO in low magnetic field region $B \leq 300$ mT. Particularly, the J_c observed in 2BZO is clearly the highest of all up to 1 T, indicating the improved crystalline quality of YBCO grown on the 5°STO substrate. However, above 1 T, the J_c of 2BZO drops significantly faster than that of 4BZO. Above 3 T, there is also a crossover in J_c between the films 4BZO and 6BZO, leading to the fact that the highest $J_c(B)$ in the high magnetic field range is in sample 6BZO. In the samples 8BZO and 10BZO, J_c is higher above 0.2 and 0.8 T, respectively, when compared with the sample 0BZO, even though they show extremely poor J_c behavior in the low-field region. The crossovers visible in the J_c curves at high fields between different samples indicate the effectiveness of the defect density with the higher BZO concentrations. When looking at the $J_c(B)$ curves of films on STO in Figure 4(b), the highest self-field $J_c(0)$ can be observed in film 0BZO, while the highest $J_c(B)$ in the high field range above 300 mT is unequivocally in sample 4BZO. Obtaining the difference between the samples grown on 5°STO and STO substrates at 10 K (inset of Figure 4(a)), we can conclude that the self-field $J_c(0)$ is clearly increased in 5°STO in all of the samples containing BZO doping, and the in-field $J_c(B)$ is also improved in films grown on 5°STO when the BZO dopant concentration exceeds 4%. In addition, the low-field plateau of $J_c(0)$ is clearly lengthened in 5°STO samples regardless of the BZO doping, as can be seen in the inset of Figure 4(b).

Summarizing the temperature-dependent J_c at different magnetic fields, we have collected histograms illustrating the improvement of J_c in 5°STO samples when compared with the samples grown on a traditional STO substrate. When looking at the results at 10 K, the samples 5°STO generally beat all of the BZO-doped samples deposited on STO, with 60−80% improvement in sample 10BZO in a wide magnetic field range

https://doi.org/10.1021/acs.cgd.3c00768
Cryst. Growth Des. XXXX, XXX, XXX−XXX

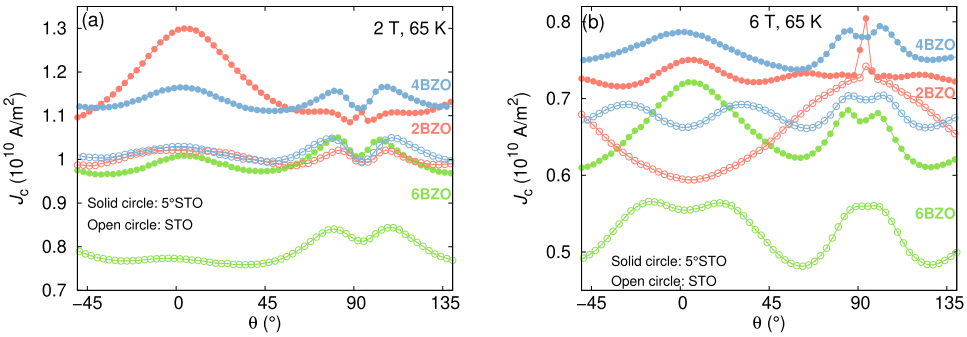

Figure 6. Resistively measured critical current anisotropies for samples with varying BZO concentrations measured at 65 K under applied field of 2 T (a) and 6 T (b).

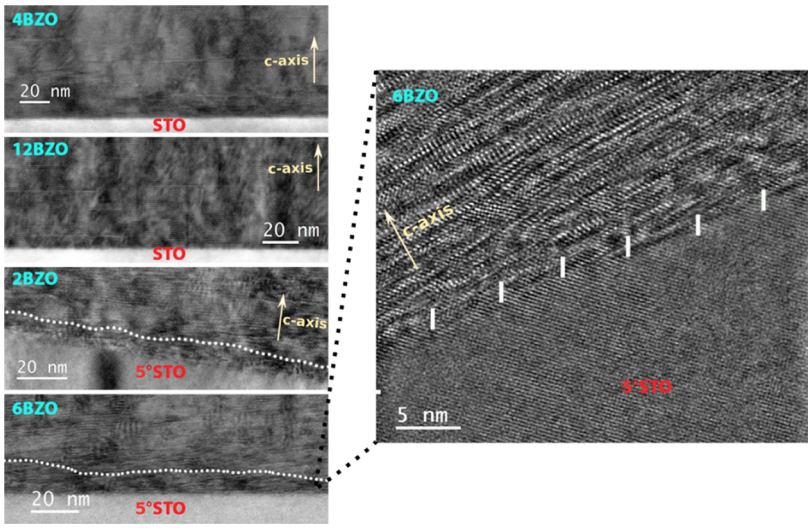

Figure 7. Cross-sectional STEM images for the substrate/film interface between 4BZO/STO, 12BZO/STO, 2BZO/5°STO, and 6BZO/5°STO. The white dotted line indicates the strained region next to the 5°STO substrate interface, and the yellow arrow indicates the *c*-axis direction of YBCO. The magnified image of interface between 6BZO/5°STO substrate and the terrace widths (4.92−5.99 nm) are also presented on the right panel.

up to 3 T. The predominance of 5°STO samples is even more pronounced at a high temperature of 65 K, where especially at high BZO concentrations the superiority is emphasized, having for example almost 200% improvement in 6% BZO-doped sample measured in field of 1 T. It is good to mention that at high temperatures the greater improvement in J_c is obtained already at lower BZO concentrations, and thus clearly the best BZO content of 4% in films on STO substrates loses its meaning when using the vicinal substrates. The results indicate that both crystalline quality and flux pinning are obviously improved in films grown on 5°STO substrates, especially at high BZO concentrations. These are in good agreement with our TEM results, where longer and significantly splayed BZO nanorods together with slightly tilted stacking faults have been observed in 5°STO films.

Angular-Dependent Flux Pinning. To investigate the vortex pinning landscape in 5°STO and STO films, the angular-dependent critical current densities were measured at temperatures of 10 and 65 K and in magnetic fields up to 8 T. As can be seen in Figure 5, the correlated pinning related to the BZO nanorods is clearly visible in both 5°STO and STO samples, since clear evolution of the peak in both directions, the magnetic field parallel to the YBCO *c*-axis (θ = 0°) and parallel to the YBCO *ab*-plane (θ = 90°), is obvious. When looking at the absolute values of $J_c(\theta)$ at 10 K, the 5°STO samples demonstrate better J_c performance throughout the full angular range, not only along the BZO nanorods in parallel to the YBCO *c*-axis. In addition, the variation in the sizes and shapes of the peaks of $J_c(\theta)$ in samples 2BZO, 4BZO, and 6BZO clearly has magnetic field dependence, as illustrated in Figure 5(a,b).

In the 2 T field, the 2BZO film has a greatly increased *c*-axis peak in the 5°STO sample, while the peak shapes do not remarkably change in either the 5°STO or STO samples with 4 and 6% BZO concentrations. Evidently, 4 and 6% BZO samples on both substrates exhibit a dip in $J_c(\theta)$ along the *ab*-plane, accompanied by distinct shoulders, which may be attributed to the fluctuating step length of vortices along the *ab*-plane, particularly when a sparse population of vortices is present at lower magnetic fields.[44]

Instead, the results at 6 T show that the highest *c*-axis peak is in 6BZO 5°STO sample and $J_c(\theta)$ curves of STO exhibit a clear double peak along the *c*-direction for both 4BZO and 6BZO samples, while 2BZO displays nearly flat angular dependence of J_c. Obviously, the $J_c(\theta)$ curves of 5°STO show the absence of peaks along the *c*-axis when the BZO concentration increases to 8 and 10%, as shown in Figure 5(c). However, a broad J_c peak along the *ab*-plane is observed in 5°STO samples with 8 and 10% BZO concentrations, indicating enhanced correlated pinning along the in-plane

https://doi.org/10.1021/acs.cgd.3c00768
Cryst. Growth Des. XXXX, XXX, XXX−XXX

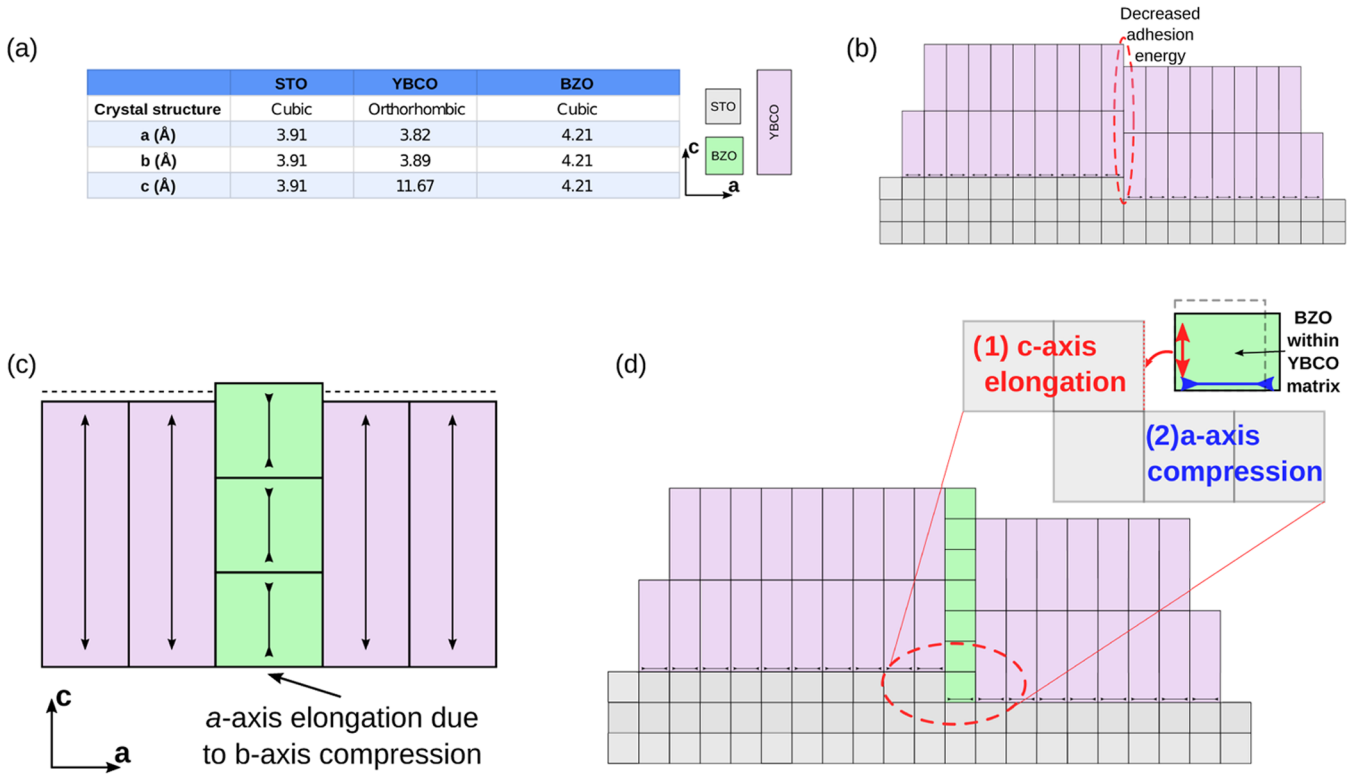

	STO	YBCO	BZO
Crystal structure	Cubic	Orthorhombic	Cubic
a (Å)	3.91	3.82	4.21
b (Å)	3.91	3.89	4.21
c (Å)	3.91	11.67	4.21

Figure 8. (a) Tabulated lattice parameters of YBCO, BZO, and STO unit cells, along with a schematic illustration of their relative sizes along the *a* and *c*-directions. (b) Schematic illustration of pure YBCO grown on the vicinal STO substrate. The step-edge can be considered to induce lattice defects in its vicinity. (c) Illustration of BZO unit cells within the YBCO matrix. (d) Illustration of YBCO + *x*%BZO growth on the vicinal STO substrate. The formation of BZO nanorods is enhanced by the step edges, consequently enhancing the overall crystalline quality of the surrounding YBCO.

direction. Contrarily, the nanocolumns in STO samples with higher BZO content serve as a strong pinning source for vortices with magnetic field applied along the *c*-axis, leading to a more pronounced J_c peak in the *c*-axis direction, especially in the high field range.

Consequently, the $J_c(\theta)$ curves of 8 and 10% BZO-doped STO films display a more pronounced J_c peak in the *c*-direction at 6 T when compared with the 5°STO samples, as demonstrated in Figure 5(d). This is nicely in accordance with our TEM finding, where the nanorods start to deviate from the direction of the *c*-axis to the *ab*-plane direction in 5°STO samples with high BZO concentrations, resulting in stronger effective pinning along the *ab*-plane and broader *ab*-peak as seen in the $J_c(\theta)$ curves.

As the temperature rises to 65 K, as shown in Figure 6(a), the $J_c(\theta)$ peaks along the YBCO *c*-axis in STO films experience a drastic decrease at 2 T. Notably, the 5°STO samples exhibit distinct *c*-axis peaks in $J_c(\theta)$ curves of 2BZO, 4BZO and 6BZO dopant concentrations in both magnetic fields 2 and 6 T. At the 6 T field, the clearly separated double peaks in the $J_c(\theta)$ curves for STO 4BZO and 6BZO samples can be seen, while 2BZO exhibits an almost concave curve. We can conclude that the combination of substrate miscut and real lattice mismatch in 5°STO samples induces significantly enhanced strain, leading to improved BZO nanorod configurations and stronger flux pinning, which also results in clearly improved $J_c(\theta)$ performance when compared with the films deposited on STO(100) substrates.

Improved Flux Pinning by Step-Edge Strain-Induced BZO Nanorod Growth. In the STO film, the predominantly semicoherent interface strain[10,45,46] caused by YBCO/BZO leads to a decrease in the overall quality of the YBCO matrix between the BZO nanorods. This is due to the formation of a high density of misfit dislocations. The film/substrate strain plays a minor role (Figure 7). However, in the vicinal film, the substrate/film interface strain behaves differently. The miscut of the substrate results in clearly visible tetragonally distorted substrate terraces and anisotropic crystallinity. This is in contrast to the isotropic strain observed in YBCO grown on well-oriented STO substrates. As a result, there is a stronger deviation from the perfect alignment of the *c*-axis in the orthogonal direction of the interface region. The step edges of the YBCO film exhibit waviness and meandering, which are distinct from those in the (100) oriented substrates. These observations are consistent with the substantial broadening of X-ray diffraction rocking curves observed in the 5°STO film.

The microstructure of the films improves as the distance from the substrate increases. The required layer thickness for microstructure relaxation significantly exceeds the critical thickness of *c*-axis-oriented YBCO films on pristine STO.[47] Unlike the pristine substrate, the additional strain induced by the miscut substrate, anisotropic crystallinity, and mismatch between the film unit cells and substrate terrace width cannot be released through edge dislocations. Therefore, this strain is stored in the epitaxial films. Furthermore, the step-flow growth of YBCO on 5°STO[48] reduces the likelihood of developing defects compared to the island growth mechanism. In conclusion, the strain relaxation in YBCO is less pronounced, which restricts the formation of defects and facilitates improved growth of BZO nanorods in both in-plane and

https://doi.org/10.1021/acs.cgd.3c00768
Cryst. Growth Des. XXXX, XXX, XXX−XXX

out-of-plane directions. This is supported by larger YBCO strain values and narrower BZO $\omega(002)$ and $\phi(110)$ peaks in films on the vicinal substrate. The improved growth is achieved by reduced mismatch strain between YBCO and BZO, leading to the preservation of a coherent interface between these two materials.

To understand the differences between the undoped and BZO-doped YBCO films on normal STO(100) and 5° vicinally cut STO substrates, we concentrate on two experimentally observed features that can be considered to be rather self-evident. First, the fact that pure YBCO has increased superconducting properties on normal STO when compared with the 5°STO can be easily related to the step-like structure of the vicinal substrate. Since $c_{YBCO} \gg c_{STO}$ (Figure 8(a)), dislocations and other defects are more probably formed in the vicinity of the steps due to decreased adhesion energies of the YBCO unit cells as schematically illustrated in Figure 8(b). Thus, the overall crystalline quality can be expected to be decreased, which is directly reflected in the observed decreased T_c and $J_{c,0}$ for the vicinal substrate when compared to the normal one. Second, the linear decrease of $J_{c,0}$ as a function of BZO concentration, which is observed for both substrates (Figure 4(a)), can be approximately explained by the reduced superconducting cross-sectional area.[49] That is, increasing the amount of nonsuperconducting BZO decreases the superconducting cross-sectional area for the supercurrent to pass through. Since the $J_{c,0}$ is nevertheless derived by measuring the critical current ($I_{c,0}$) and the overall dimensions of the associated film, the linear decrease of $J_{c,0}$ as a function of BZO concentration evidently follows. Obviously, the nanorod-induced strain also degrades the superconducting properties, but this effect is elusive to estimate quantitatively. However, this could be considered to be incorporated within the above-described simplified model.[49]

The remaining question is why the BZO-doped YBCO grows better on the vicinal substrate and in particular for the higher BZO concentrations. Obviously, this has to be related to the interaction between the BZO unit cell and the step-like structure of the vicinal substrate. Perhaps the simplest quantitatively assessable physical quality related to the quality of the film growth is the critical thickness (t_c), defining the thickness above which the substrate-induced strain is released by the formation of dislocations. The t_c is ultimately determined by the lattice mismatch (f) between the substrate and the film, and by the simplest approximation $t_c \propto f^{-1}$.[50] We argue that the quality of the BZO nanorod growth correlates with the associated t_c for BZO, which again is reflected in the overall quality of the surrounding YBCO matrix. In order to address this more quantitatively, the lattice parameters of the associated unit cells need to be evaluated.

The effective c-parameter within the YBCO + x%BZO superlattice can be calculated as the geometric average of the c-axis parameters associated with the individual YBCO and BZO unit cells, resulting in

$$c_{eff} = x\cdot(3\cdot c_{BZO}) + (1 - x)\cdot c_{YBCO} \quad (1)$$

where we have taken into consideration that $c_{YBCO} \approx 3 \cdot c_{BZO}$ as schematically illustrated in Figure 8(c). Thus, the effective c-parameter for a single BZO unit cell within the superlattice is $c'_{BZO} = c_s/3$. Similarly, one can calculate the effective b-parameter as

$$b_{eff} = x\cdot b_{BZO} + (1 - x)\cdot b_{YBCO} \quad (2)$$

The YBCO-induced strain along the b-axis affects the a-parameter of the BZO unit cell according to the Poisson ratio ($\nu \approx 0.3$) as

$$a'_{BZO} = a_{BZO} + 2\cdot(b_{BZO} - b_{eff})\cdot\nu \quad (3)$$

On a normal STO substrate, the corresponding lattice mismatch would be $f_n = (a'_{BZO} - a_{STO})/a_{STO}$. However, on the vicinal substrate, the BZO a-parameter is further modified as the step-edge of the substrate strains the BZO along the c-direction as illustrated in Figure 8(d). A simple calculation reveals that the step height of the 5° cut STO substrate corresponds to a single STO unit cell (c_{STO}). Consequently, the BZO a-parameter is changed to

$$a''_{BZO} = a'_{BZO} + 2\cdot(c_{eff}/3 - c_{STO})\cdot\nu \quad (4)$$

and the associated lattice mismatch becomes $f_v = (a''_{BZO} - a_{STO})/a_{STO}$. Figure 9 presents the evaluated lattice mismatches

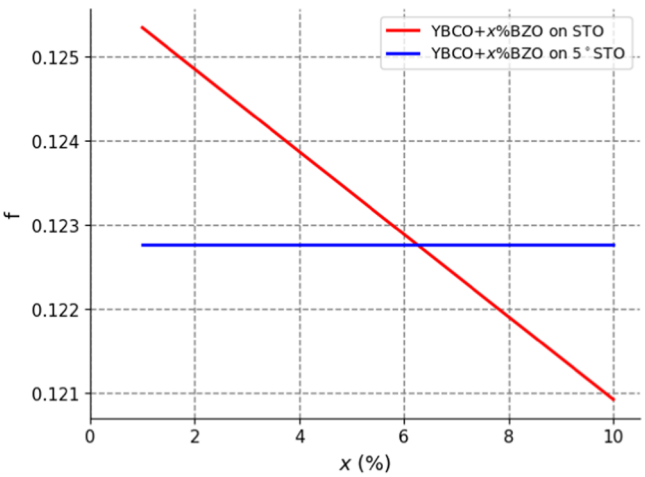

Figure 9. Evaluated lattice mismatches of YBCO+x%BZO as a function of dopant concentration on normal and vicinal substrates.

of YBCO + x%BZO superlattices as a function of the dopant concentration x based on the above considerations. While f decreases linearly as a function of the dopant concentration for normal substrate, in the case of the vicinal substrate the f remains approximately constant. As a result, the f is smaller for the vicinal substrate when compared with the normal one up to $x \approx 6\%$. This suggests that the crystalline quality of YBCO + x %BZO would be increased on the vicinal substrate when compared with the normal one for dopant concentrations $x < 6\%$, excluding $x = 0\%$. Above this limit, the normal substrate would be more preferable when the crystalline quality of the film. This is in slight contradiction with the experimentally observed results, where the superconducting properties of YBCO + x%BZO were observed to be increased on vicinal substrates for all measured $x > 0\%$. This can be attributed to the fact that the nanorods are not exclusively composed of BZO, but they also contain distorted YBCO or other compounds. The phenomenon also explains the observed difference between the BZO content and the nanorod density.[10,13,51] In this case, the observed results would coincide with the experimental observations in the sense that the YBCO + x%BZO can be concluded to grow better on the vicinal substrate.

In summary, our calculations suggest that the step edges within the vicinal substrate strain the BZO unit cells along the

https://doi.org/10.1021/acs.cgd.3c00768
Cryst. Growth Des. XXXX, XXX, XXX−XXX

c-direction resulting in decreased lattice mismatch along the *ab*-plane. This leads to better formation of the BZO nanorods and is reflected in the improved superconducting properties of YBCO + *x*%BZO superlattices on vicinal substrates when compared with normal ones.

CONCLUSIONS

The research presented in this article highlights the significant advancements in controlled BZO nanorod growth and the subsequent improvements in flux pinning observed in YBCO films grown on vicinally miscut STO substrates. Through a detailed analysis of the structural and superconducting properties, we have established several key findings related to the successful manipulation of nanorod alignment and density, leading to enhanced vortex pinning and critical current density in the superconducting films.

First, the utilization of vicinal substrates has led to improved BZO nanorod growth. These nanorods exhibit slightly greater diameters, increased lengths, and more extensive penetration through the YBCO film. Furthermore, they are found to be more randomly distributed and significantly splayed, which enhances flux pinning. Second, the superconducting properties of YBCO films grown on vicinal STO substrates exhibit substantial improvements. Both the zero- and in-field critical current densities demonstrate remarkable enhancements across a wide temperature range and in the presence of external magnetic fields. This signifies the effectiveness of utilizing vicinal substrates in promoting superior superconducting behavior. Lastly, we propose a semiquantitative model that provides insights into the underlying mechanisms responsible for the observed improvements in flux pinning. This model suggests that the enhanced flux pinning is attributed to the combined effects of step-edge strain and modified lattice-mismatch-induced BZO nanorod growth. These factors contribute to the formation of an optimized pinning landscape, resulting in the observed improvements in the critical current densities.

Overall, our findings highlight the significance of utilizing vicinal STO substrates for the growth of YBCO films with improved flux pinning properties. This is particularly significant because it can be linked to the coated conductor technology, where the IBAD process generates an inclined surface that corresponds to the vicinal substrates. These results contribute to advancing our understanding of flux pinning mechanisms and pave the way for the development of more efficient superconducting devices with enhanced critical current densities.

AUTHOR INFORMATION

Corresponding Authors

Moe Moe Aye − *Wihuri Physical Laboratory, Department of Physics and Astronomy, University of Turku, 20014 Turku, Finland; University of Turku Graduate School (UTUGS), University of Turku, 20014 Turku, Finland;* orcid.org/0000-0001-8021-118X; Email: moe.m.aye@utu.fi

Elmeri Rivasto − *Wihuri Physical Laboratory, Department of Physics and Astronomy, University of Turku, 20014 Turku, Finland; University of Turku Graduate School (UTUGS), University of Turku, 20014 Turku, Finland;* Email: elmeri.o.rivasto@utu.fi

Authors

Hannes Rijckaert − *SCRiPTS, Department of Chemistry, Ghent University, 9000 Ghent, Belgium;* orcid.org/0000-0002-6078-2919

Hannu Huhtinen − *Wihuri Physical Laboratory, Department of Physics and Astronomy, University of Turku, 20014 Turku, Finland*

Isabel Van Driessche − *SCRiPTS, Department of Chemistry, Ghent University, 9000 Ghent, Belgium;* orcid.org/0000-0001-5253-3325

Petriina Paturi − *Wihuri Physical Laboratory, Department of Physics and Astronomy, University of Turku, 20014 Turku, Finland*

Complete contact information is available at: https://pubs.acs.org/10.1021/acs.cgd.3c00768

Notes

The authors declare no competing financial interest.

ACKNOWLEDGMENTS

The Jenny and Antti Wihuri Foundation and the University of Turku Graduate School are acknowledged for financial support. TEM measurements were carried out at the UGent TEM Core Facility. Hannes Rijckaert acknowledges support and funding as postdoctoral fellow fundamental research of the Research Foundation-Flanders (FWO, Grant number 1273621N).

REFERENCES

(1) Goyal, A.; Kang, S.; Leonard, K. J.; Martin, P. M.; Gapud, A. A.; Varela, M.; Paranthaman, M.; Ijadoula, A. O.; Specht, E. D.; Thompson, J. R.; Christen, D. K.; Pennycook, S. J.; List, F. A. Irradiation free, columnar defects comprised of self-assembled nanodots and nanorods resulting in strongly enhanced flux pinning in $YBa_2Cu_3O_{7-\delta}$ films. *Supercond. Sci. Technol.* **2005**, *18*, 1533−1538.

(2) Mele, P.; Matsumoto, K.; Horide, T.; Ichinose, A.; Mukaida, M.; Yoshida, Y.; Horii, S.; Kita, R. Ultra-high flux pinning properties of $BaMO_3$-doped $YBa_2Cu_3O_{7-x}$ thin films (M = Zr, Sn). *Supercond. Sci. Technol.* **2008**, *21*, No. 032002.

(3) MacManus-Driscoll, J. L.; Foltyn, S. R.; Jia, Q. X.; Wang, H.; Serquis, A.; Civale, L.; Maiorov, B.; Hawley, M. E.; Maley, M. P.; Peterson, D. E. Strongly enhanced current densities in superconducting coated conductors of $YBa_2Cu_3O_{7-x}$ + $BaZrO_3$. *Nat. Mater.* **2004**, *3*, 439−443.

(4) Yamada, Y.; Takahashi, K.; Kobayashi, H.; Konishi, M.; Watanabe, T.; Ibi, A.; Muroga, T.; Miyata, S.; Kato, T.; Hirayama, T.; Shiohara, Y. Epitaxial nanostructure and defects effective for pinning in $Y(RE)Ba_2Cu_3O_{7-x}$ coated conductors. *Appl. Phys. Lett.* **2005**, *87*, No. 132502.

(5) Haugan, T.; Barnes, P. N.; Wheeler, R.; Meisenkothen, F.; Sumption, M. Addition of nanoparticle dispersions to enhance flux pinning of the $YBa_2Cu_3O_{7-x}$ superconductor. *Nature* **2004**, *430*, 867−870.

(6) Mele, P.; Matsumoto, K.; Horide, T.; Ichinose, A.; Mukaida, M.; Yoshida, Y.; Horii, S. Insertion of nanoparticulate artificial pinning centres in $YBa_2Cu_3O_{7-x}$ films by laser ablation of a Y_2O_3-surface modified target. *Supercond. Sci. Technol.* **2007**, *20*, 616−620.

(7) Krusin-Elbaum, L.; Marwick, A. D.; Wheeler, R.; Feild, C.; Vinokur, V. M.; Leaf, G. K.; Palumbo, M. Enhanced Pinning with Controlled Splay Configurations of Columnar Defects; Rapid Vortex Motion at Large Angles. *Phys. Rev. Lett.* **1996**, *76*, 2563−2566.

(8) Horide, T.; Sakamoto, N.; Ichinose, A.; Otsubo, K.; Kitamura, T.; Matsumoto, K. Hybrid artificial pinning centers of elongated-nanorods and segmented- nanorods in $YBa_2Cu_3O_7$ films. *Supercond. Sci. Technol.* **2016**, *29*, No. 105010.

(9) Emergo, R. L. S.; Baca, F. J.; Wu, J. Z.; Haugan, T. J.; Barnes, P. N. The effect of thickness and substrate tilt on the BZO splay and superconducting properties of $YBa_2Cu_3O_{7-\delta}$films. *Supercond. Sci. Technol.* **2010**, *23*, No. 115010.
(10) Cantoni, C.; Gao, Y.; Wee, S. H.; Specht, E. D.; Gazquez, J.; Meng, J.; Pennycook, S. J.; Goyal, A. Strain-driven oxygen deficiency in self-assembled, nanostructured, composite oxide films. *ACS Nano* **2011**, *5*, 4783−4789.
(11) Kang, S.; Goyal, A.; Li, J.; Martin, P.; Ijaduola, A.; Thompson, J. R.; Paranthaman, M. Flux-pinning characteristics as a function of density of columnar defects comprised of self-assembled nanodots and nanorods in epitaxial $YBa_2Cu_3O_{7-\delta}$ films for coated conductor applications. *Phys. C* **2007**, *457*, 41−46.
(12) Peurla, M.; Paturi, P.; Stepanov, Y. P.; Huhtinen, H.; Tse, Y. Y.; Bódi, A. C.; Raittila, J.; Laiho, R. Optimization of the $BaZrO_3$ concentration in YBCO films prepared by pulsed laser deposition. *Supercond. Sci. Technol.* **2006**, *19*, 767−771.
(13) Peurla, M.; Huhtinen, H.; Shakhov, M. A.; Traito, K.; Stepanov, Y. P.; Safonchik, M.; Paturi, P.; Tse, Y. Y.; Palai, R.; Laiho, R. Effects of nanocrystalline target and columnar defects on flux pinning in pure and BZO-doped YBCO films in fields up to 30 T. *Phys. Rev. B* **2007**, *75*, No. 184524.
(14) Aye, M. M.; Rivasto, E.; Rijckaert, H.; Palonen, H.; Huhtinen, H.; Van Driessche, I.; Paturi, P. Optimized $BaZrO_3$ nanorod density in $YBa_2Cu_3O_{6+x}$ matrix for high field applications. *Supercond. Sci. Technol.* **2022**, *35*, No. 075006, DOI: 10.1088/1361-6668/ac6cac.
(15) Wu, J. Z.; nd, F. J.; Baca, J. J. S.; Emergo, R.; Wilt, J.; Haugan, T. J. Controlling $BaZrO_3$ nanostructure orientation in $YBa_2Cu_3O_{7-\delta}$ films for a three-dimensional pinning landscape. *Supercond. Sci. Technol.* **2015**, *28*, No. 125009.
(16) Haage, T.; Zegenhagen, J.; Li, J. Q.; Habermeier, H.-U.; Cardona, M. Transport properties and flux pinning by self-organization in YBCO films on vicinal $SrTiO_3$ (001). *Phys. Rev. B* **1997**, *56*, No. 8404.
(17) Haage, T.; Zegenhagen, J.; Jooss, C.; Warthmann, R.; Li, J. Q.; Habermeier, H.-U.; Cardona, M. Nanoscale engineering: Tailored properties by self-organization in $YBa_2Cu_3O_{7-\delta}$ thin films. *Phys. C* **1997**, *282*−*287*, 557−558.
(18) Emergo, R. L. S.; Wu, J. Z.; Aytug, T.; Christen, D. K. Thickness dependence of superconducting critical current density in vicinal $YBa_2Cu_3O_{7-\delta}$ thick films. *Appl. Phys. Lett.* **2004**, *85*, 618−620.
(19) Chakalova, R. I.; Jackson, T. J.; Passerieux, G.; Jones, I. P.; Mikheenko, P.; Muirhead, C. M.; Darlington, C. N. W. Effect of substrate vicinality on the formation of precipitates and twins in YBCO thin films. *Phys. Rev. B* **2004**, *70*, No. 214504.
(20) Mechin, L.; Berghuis, P.; Evetts, J. Properties of $YBa_2Cu_3O_{7-\delta}$ thin films grown on vicinal $SrTiO_3$ (001) substrates. *Phys. C* **1998**, *302*, 102−112.
(21) Kim, J.; Chrisey, D.; Horwitz, J.; Miller, M.; Gilmore, C. Growth mechanism of $YBa_2Cu_3O_{7-\delta}$ thin films and precipitates on planar and vicinal $SrTiO_3$ substrates. *J. Mater. Res.* **2000**, *15*, 596−613.
(22) Brötz, J.; Fuess, H.; Haage, T.; Zegenhagen, J.; Jooss, C.; Forkl, A.; Warthmann, R. Anisotropic defect structure and transport properties of $YBa_2Cu_3O_{7-\delta}$ films on vicinal $SrTiO_3$(001). *J. Appl. Phys.* **1999**, *85*, 635−637.
(23) Wu, J. Z.; Emergo, R. L. S.; Wang, X.; Xu, G.; Haugan, T. J.; Barnes, P. N. Strong nanopore pinning enhances J_c*in*$YBa_2Cu_3O_{7-\delta}$ films. *Appl. Phys. Lett.* **2008**, *93*, No. 062506.
(24) Maurice, J.-L.; Briático, J.; Crété, D.-G.; Contour, J.-P. Effects of surface miscuts on the epitaxy of $YBa_2Cu_3O_{7-\delta}$ and $NdBa_2Cu_3O_{7-\gamma}$ on $SrTiO_3$(001). *Phys. Rev. B* **2003**, *68*, No. 115429.
(25) Lowndes, D. H.; Zheng, X.-Y.; Zhu, S.; Budai, J. D.; Warmack, R. J. Suppression of the spiral-growth mechanism in epitaxial $YBa_2Cu_3O_{7-\delta}$ films grown on miscut substrates. *Appl. Phys. Lett.* **1992**, *61*, 852−854.
(26) Jooss, C.; Warthmann, R.; Kronmuller, H.; Haage, T.; Habermeier, H.-U.; Zegenhagen, J. Vortex pinning due to strong quasiparticle scattering at antiphase boundaries in YBCO. *Phys. Rev. Lett.* **1999**, *82*, 632−635.
(27) Berghuis, P.; Bartolomeo, E. D.; Wagner, G. A.; Evetts, J. E. Intrinsic Channeling of Vortices along the ab Plane in Vicinal $YBa_2Cu_3O_{7-\delta}$ films. *Phys. Rev. Lett.* **1997**, *79*, 2332−2335.
(28) Brötz, J.; Fuess, H.; Haage, T.; Zegenhagen, J. Controlled modification of interfacialstrain and twinning in YBa2 $Cu_3O_{7-\delta}$ films on vicinal $SrTiO_3$ (001). *Phys. Rev. B* **1998**, *57*, No. 3679.
(29) Durrell, J. H.; Evetts, J. E.; Rössler, R.; Delamare, M. P.; Pedarnig, J. D.; Bäuerle, D. Effect of varying material anisotropy on critical current anisotropy in vicinal $YBa_2Cu_3O_{7-\delta}$ thin films. *Appl. Phys. Lett.* **2003**, *83*, 4999−5001.
(30) Yao, G.; Gao, M.; Ji, Y.; Liang, W.; Gao, L.; Zheng, S.; Wang, Y.; Pang, B.; Chen, Y. B.; Zeng, H.; Li, H.; Wang, Z.; Liu, J.; Chen, C.; Lin, Y. Surface step terrace tuned microstructures and dielectric properties of highly epitaxial $CaCu_3Ti_4O_{12}$ thin films on vicinal $LaAlO_3$ substrates. *Sci. Rep.* **2016**, *6*, No. 34683.
(31) Baca, F. J.; Barnes, P. N.; Emergo, R. L. S.; Haugan, T. J.; Reichart, J. N.; Wu, J. Z. Control of BZO nanorod alignment in YBCO thin films by microstructural modulation. *Appl. Phys. Lett.* **2009**, *94*, No. 102512.
(32) Baca, F. J.; Emergo, R. L.; Wu, J. Z.; Haugan, T. J.; Reichart, J. N.; Barnes, P. N. Microstructural characterization of $YBa_2Cu_3O_{7-\delta}$ films with $BaZrO_3$ nanorods grown on vicinal $SrTiO_3$ substrates. *IEEE Trans. Appl. Supercond.* **2009**, *19*, 3371−3374.
(33) Kim, C.; Robinson, I. K.; Myoung, J.; Shim, K.; Yoo, M.-C.; Kim, K. Critical thickness of GaN thin films on sapphire (0001). *Appl. Phys. Lett.* **1996**, *69*, 2358−2360.
(34) Fischer, A.; Kühne, H.; Richter, H. New approach in equilibrium theory for strained layer relaxation. *Phys. Rev. Lett.* **1994**, *73*, 2712−2715.
(35) Wiesinger, H. P.; Sauerzopf, F. M.; Weber, H. W. On the calculation of J_c from magnetization measurements on superconductors. *Phys. C* **1992**, *203*, 121−128.
(36) Polyanskii, A.; Emergo, R. L. S.; Wu, J. Z.; Aytug, T.; Christen, D. K.; Perkins, G. K.; Larbalestier, D. Magneto-optical imaging and electromagnetic study of $YBa_2Cu_3O_7$ vicinal films of variable thickness. *Phys. Rev. B* **2005**, *72*, No. 174509.
(37) Cantoni, C.; Verebelyi, D. T.; Specht, E. D.; Budai, J.; Christen, D. K. Anisotropic nonmonotomic behavior of the superconducting critical current in thin YBCO films on vicinal $SrTiO_3$. *Phys. Rev. B* **2005**, *71*, No. 054509.
(38) Polyanskii, A. A.; Gurevich, A.; Pashitski, A. E.; Heinig, N. F.; Redwing, R. D.; Nordman, J. E.; Larbalestier, D. Magneto-optical study of flux penetration and critical current densities in [001] tilt YBCO thin film bicrystals. *Phys. Rev. B* **1996**, *53*, 8687−8697.
(39) Jia, Q. X.; Foltyn, S. R.; Arendt, P. N.; Smith, J. F. High-temperature superconducting thick films with enhanced supercurrent carrying capability. *Appl. Phys. Lett.* **2002**, *80*, 1601−1603.
(40) Yeh, N. C.; Kriplani, U.; Jiang, W.; Reed, D. S.; Strayer, D. M.; Barner, J. B.; Hunt, B. D.; Foote, M. C.; Vasquez, R. P.; Gupta, A.; Kussmaul, A. Microwave vortex dissipation of superconducting Nd-Ce-Cu-O epitaxial films in high magnetic fields. *Phys. Rev. B* **1993**, *48*, 9861−9864.
(41) Rivasto, E.; Khan, M. Z.; Malmivirta, M.; Rijckaert, H.; Aye, M. M.; Hynninen, T.; Huhtinen, H.; Driessche, I. V.; Paturi, P. Self-assembled nanorods in YBCO matrix - a computational study of their effects on critical current anisotropy. *Sci. Rep.* **2020**, *10*, No. 3169.
(42) Aye, M. M.; Rivasto, E.; Khan, M. Z.; Rijckaert, H.; Palonen, H.; Huhtinen, H.; Van Driessche, I.; Paturi, P. Multilayering BZO nanocolumns with different defect densities for YBCO high field applications. *New J. Phys.* **2021**, *23*, No. 113031.
(43) Wu, J.; Shi, J. Interactive modeling-synthesis-characterization approach towards controllable in situ self-assembly of artificial pinning centers in RE-123 films. *Supercond. Sci. Technol.* **2017**, *30*, No. 103002.
(44) Paturi, P. The vortex path model and angular dependence of J_c in thin YBCO films deposited from undoped and $BaZrO_3$-doped targets. *Supercond. Sci. Technol.* **2010**, *23*, No. 025030.
(45) Gautam, B.; Sebastian, M. A.; Chen, S.; Haugan, T.; Zhang, W.; Huang, J.; Wang, H.; Wu, J. Microscopic adaptation of $BaHfO_3$ and

Y_2O_3 artificial pinning centers for strong and isotropic pinning landscape in $YBa_2Cu_3O_{7-x}$ thin films. *Supercond. Sci. Technol.* **2018**, *31*, No. 025008.
(46) Ogunjimi, V.; Gautam, B.; Sebastian, M. A.; Haugan, T.; Wu, J. The effect of APC/YBCO interface on the angular range of effective pinning by one-dimensional artificial pinning centers in YBa_2 Cu_3 O_{7-x} nanocomposite films. *Mater. Sci. Eng.* **2020**, *756*, No. 012025.
(47) Pedarnig, J. D.; Rössler, R.; Delamare, M. P.; Lang, W.; Bäuerle, D.; et al. Electrical properties, texture, and microstructure of vicinal $YBa_2Cu_3O_{7-\delta}$ thin films. *Appl. Phys. Lett.* **2002**, *81*, 2587−2589.
(48) Lowndes, D. H.; Zheng, X.-Y.; Zhu, S.; Budai, J. D.; Warmack, R. J. Suppression of the spiral-growth mechanism in epitaxial $YBa_2Cu_3O_{7-x}$ films grown on miscut substrates. *Appl. Phys. Lett.* **1992**, *61*, 852−854.
(49) Rivasto, E.; Hynninen, T.; Huhtinen, H.; Paturi, P. Optimization of high-temperature superconducting bilayer structures using a vortex dynamics simulation. *J. Phys. Cond. Mater.* **2023**, *35*, No. 075701.
(50) Matthews, J. W.; Blakeslee, A. E. Defects in epitaxial multilayers: I. Misfit dislocations. *J. Cryst. Growth* **1974**, *27*, 118−125.
(51) Majkic, G.; Jeong, J. S.; Yun, H.; Hernandez, F. C. R.; Galstyan, E.; Pratap, R.; Cheng, H.; Stokes, A.; Mkhoyan, K. A.; Selvamanickam, V. New insight into strain and composition of $BaZrO_3$ nanorods in REBCO superconductor. *Supercond. Sci. Technol.* **2021**, *34*, No. 115002.

https://doi.org/10.1021/acs.cgd.3c00768
Cryst. Growth Des. XXXX, XXX, XXX−XXX